http://dx.doi.org/10.1016/j.ijmecsci.2021.106503

A multiscale constitutive model coupled with martensitic transformation kinetics for micro-scaled plastic deformation of metastable metal foils

B. Meng[1], Y.Z. Liu[1], M. Wan[1], M.W. Fu[2, *]

[1]School of Mechanical Engineering and Automation, Beihang University, Beijing 100191, P.R. China

[2]Department of Mechanical Engineering, The Hong Kong Polytechnic University, Hung Hom, Kowloon, Hong Kong, P.R. China

[*]Corresponding author. Tel.: 852-27665527. E-mail address: mmmwfu@polyu.edu.hk

Abstract

The mechanical behavior of metastable austenitic foils at the size scale from micron to submillimeter is strongly affected by the coupling between size effect and strain-induced martensitic transformation (SIMT), which remains to be a pressing issue to be explored. In this research, the focus is on developing a multiscale constitutive model to reveal the mechanical behavior of metastable foils and more accurately predict the size effect on SIMT. In tandem with this, the martensitic transformation and hardening behavior of SUS304 foils with different thicknesses and grain sizes were explored. The results figured out that the SIMT is promoted by the increase in grain size and foil thickness. Furthermore, the onset and end of stages II of work-hardening behavior are advanced and the work-hardening rate in stage II increases faster with increasing grain size and foil thickness. The SIMT kinetic model was coupled with the intermediate mixture law and the iso-work hypothesis to identify the stress-strain relationship of individual austenite and martensite at the surface and interior layers, which was used to construct the multiscale constitutive model. The multiscale model was developed based on the framework of the surface layer model and the intermediate mixture law to represent the coupling between the size effect and the SIMT. Through finite element simulation by using the proposed multiscale constitutive model, the dispersion hardening mechanism in micro-scaled deformation of metastable austenitic foils caused by the non-homogeneous plastic deformation at the interface between austenite and martensite was revealed. The multiscale model was validated via the corroboration of finite element simulation with experiments and therefore can provide a robust analysis of the micro-scaled deformation behavior of metastable austenitic foils.

Keywords: Multiscale constitutive model; Strain-induced martensitic transformation; Size effect; Micro-scaled plastic deformation; Metastable metal foils.

1. Introduction

The increasing demand for micro-scaled products in different industrial clusters presents crucial and pressing challenges in terms of the reliability and effectiveness of microforming technologies [1]. Due to the size effect, the fabrication of micro-scaled parts and components is still one of the bottleneck issues in the present metal forming area [2]. Recently, the size effect affected deformation behaviors have been extensively explored in terms of flow stress [3], ductile fracture [4], plastic anisotropy [5], and subsequent yield [6]. However, the size effect in the micro-scaled deformation of metastable metal foils is rarely reported due to the occurrence of the phase transformation.

Due to the desirable mechanical properties and corrosion resistance, metastable austenitic stainless steels (ASSs) have been widely used in making miniaturized parts and components, such as fuel cell bipolar plate, micro medical equipment, micro heat exchangers, and MEMS [7]. However, the mechanical properties of metastable ASSs at microscale exhibit significant difference with those at macroscale due to size effect, especially when there are only a few grains participating in deformation. Besides, the micro-scaled mechanical behavior of metastable ASSs is significantly affected by the phase transformation. The transformation from the initial face-centered cubic γ-austenite phase to the body-centered cubic α'-martensite can be triggered by the plastic deformation of metastable ASSs within a certain temperature range, which is commonly called strain-induced martensitic transformation (SIMT) [8]. The SIMT provides desirable strength and high elongation of metastable ASSs but exacerbates the difficulty of predicting mechanical behavior.

The influence of grain size at different scales on the SIMT kinetic behavior of metastable ASSs has attracted some research efforts. Varma et al. [9] and Shrinivas et al. [10] first investigated the effect of grain size ranging from 53 to 285 μm on the SIMT phenomenon of 304 ASSs during room temperature (RT) rolling and tension. They argued that the grain refinement promotes the formation of deformation-induced martensite during rolling but inhibited the SIMT during tension. Gu et al. [11] found that the onset of twinning is postponed and no twin-twin intersection occurs during the torsional deformation of a coarse-grained 304 ASS with a grain size of ~ 1000 μm compared with a fine-grained 304 ASS with a grain size of ~ 20 μm, causing the absence of the SIMT in coarse-grained materials. Matsuoka et al. [12] discussed the thermal and mechanical stability of the austenite phase in Fe–16%Cr–10%Ni steels with different grain sizes ranging from 1 to 20 μm. They concluded that the grain refinement enhances the austenitic thermal stability by inhibiting the

martensitic multi-variant transformation, while the martensitic single-variant transformation of the tensile-deformed specimen leads to the grain size independence of austenitic mechanical stability. However, some literature has reported that the austenitic mechanical stability decreases with increasing grain size. Kisko et al. [13] explored the impact of grain size ranging from 0.5 to 18 μm on the SIMT rate and nucleation sites of 204Cu steels. They elucidated that the SIMT rate increases, and the martensite nucleation sites are transferred from grain boundaries and twins to ε-martensite and shear bands with increasing grain size. Misra et al. [14] and Challa et al. [15] figured out that the deformation mechanism of 301LN ASSs shifts from transformation induced plasticity (TRIP) to twinning induced plasticity (TWIP) with the decrease of grain size ranging from 22 to 0.32 μm, which indicated that the austenitic mechanical stability is strengthened with the reduction of grain size. Therefore, the grain size effect on the mechanical stability of austenite in metastable alloys continues to be unclear.

On the other hand, the size effect on the mechanical behavior of metastable ASSs has been extensively studied in the micro-scaled deformation process [16, 17]. Nevertheless, the effect of SIMT is seldom considered. Mao et al. [18] discussed the effect of grain size ranging from 1 to 35 μm on the hardening behavior of a Fe–24%Ni–0.3%C steel and attributed the increase of work-hardening rate to the SIMT phenomenon. Naghizadeh et al. [19] revealed that coarse grains enhance the TRIP effect by promoting SIMT in 304 ASSs when the grain size is less than 50 μm. In contrast, the TRIP effect becomes less pronounced by increasing grain size for the steel with a grain size greater than 50 μm.

The modeling of macro and micro deformation behaviors of multiphase materials has been developed via three main methods including the homogenization technique like the self-consistent method, the crystal plasticity finite element method, and the phenomenological model based on the mixture law [20-22]. Compared with the first two methods, the last one is convenient for practical application, and can accurately describe and represent the mechanical response of individual constituents. However, most phenomenological models are applicable to macroscale rather than microscale since the size effect is not considered. Perlade et al. [23] developed a physical model based on an intermediate mixture law and successfully predicted the macroscopic behavior of TRIP steels. A good agreement between the simulated and the experimental evolution of the stress-strain partitioning coefficient proved the validity of the iso-work hypothesis in the intermediate mixture law. Bouquerel et al. [24] characterized the deformation behavior of multiphase TRIP

steels via a Gladman-type mixture law. They confirmed the feasibility of the developed model and derived the stress-strain distribution of different phases. Fu et al. [25] revised the index of *n* in the Gladman-type mixture law to characterize the load-stress adaptability between different phases in TRIP steels and related it to a function of martensitic transformation rate. Dan et al. [26] proposed a phenomenological model based on the intermediate mixture law and a new hypothesis that the strain energy density of multiphase steels equals the sum of that of the individual phase. They stated that the developed model could accurately describe the deformation behaviors of TRIP590 and DP590 multiphase steels.

According to the previous contributions mentioned above, most works of literature are limited to the investigation of SIMT under the macroscale scenario. The grain size effect on SIMT has not yet been fully understood, and previous reports are unavailable to reveal the interplay of geometric and grain size effects on SIMT in micro-scaled plastic deformation of metastable metal foils. In this work, comprehensive research of geometric and grain size effects on SIMT was carried out. The unique work-hardening behavior in micro-scaled deformation of metastable metal foils was explored. To describe the size-dependent SIMT and deformation response of metastable foils, a multiscale constitutive model was developed by considering the interaction of size effect and martensitic transformation, and the model was validated by experiment and finite element simulation. This study provides an in-depth understanding of SIMT under multiscale and promotes innovative findings to realize the microstructural control for micro-scaled deformation of metastable foils.

2. Experimental and simulation procedure

2.1. Specimen preparation

To explore both geometric and grain size effects on the SIMT phenomenon, the commercial SUS304 foils with thicknesses of 50, 120, and 200 μm were chosen as the test materials. The chemical composition is listed in Table 1.

Table 1 Chemical composition of SUS304 foils (in wt.%).

C	Si	Mn	P	S	Ni	Cr	Fe
0.049	0.525	1.083	0.033	0.003	8.011	18.180	Bal.

To achieve various grain sizes, the foils were annealed under different temperatures of 1000, 1050, and 1100 °C, corresponding soaking durations of 1, 1, and 1.5 h in a vacuum

oven with a vacuum degree of 10^{-3} Pa, respectively. The foils were cooled in the vacuum oven after heating and holding. The microstructure images along the cross-section were obtained by the optical microscope after etching by the solution of 10 g oxalic acid and 200 ml water, as shown in Fig. 1. The 50 μm thick foils were found to have a near-bamboo microstructure. The austenitic grain size was measured through the Heyn linear intercept method according to ASTM E112-13 standard, where twins were considered as grains. Since the grains across the thickness direction are incomplete for the 50 μm thick foil annealed at 1100 °C, the metallography along the foil plane was used to compute the average grain size under this condition. The average austenitic grain size of several sections containing about a hundred grains for each foil was computed to ensure the measurement accuracy, which is presented in Table 2. The ratio (t/d) of thickness (t) to austenitic grain size (d) of each foil is also listed in Table 2.

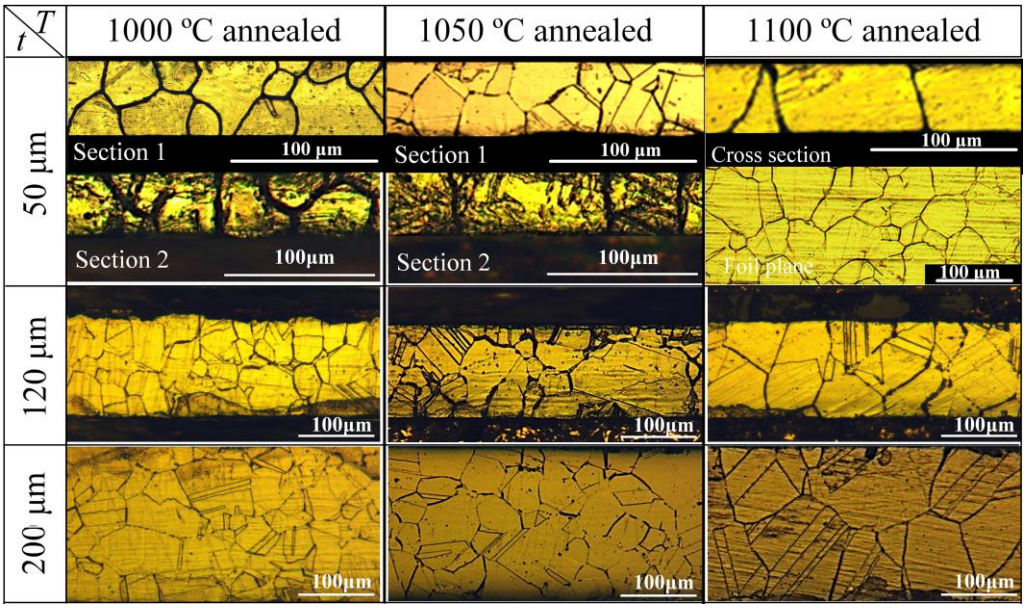

Fig. 1. Microstructures of SUS304 foils with thicknesses of 50, 120, and 200 μm after annealing at 1000, 1050, and 1100 ℃.

Table 2 Average austenitic grain size (d) and the ratio (t/d) of specimen thickness (t) to austenitic grain size (d) under various annealing conditions.

	1000 °C, 1 h		1050 °C, 1 h		1100 °C, 1.5 h	
t (μm)	d (μm)	t/d	d (μm)	t/d	d (μm)	t/d
50	21.3	2.35	52.6	0.95	69.1	0.72
120	28.7	4.18	60.3	1.99	72.7	1.65
200	29.5	6.78	64.8	3.09	94.8	2.11

2.2. Quasi-static uniaxial tension

To attain the flow behavior of metastable metal foils, the uniaxial tensile specimens with the thickness of 50 μm were prepared along the rolling direction according to ASTM E345-16 standard, while the uniaxial tensile specimens with the thicknesses of 120 and 200 μm were prepared along the rolling direction according to ASTM E8-08 standard. The gauge dimension of the tensile specimens is 50 × 12.5 mm. The tensile experiments were performed at a low strain rate of 1.6×10^{-3} s^{-1} to avoid a temperature increase induced by the plastic deformation. The digital image correlation (DIC) was adopted for the measurement of strain in the micro-scaled deformation. To ensure the reliability of experimental results, each test was repeated three times.

The martensite phase is transformed from austenite under RT plastic deformation. The deformation temperature is lower than M_d, which is the temperature above that martensite is not produced during the plastic deformation. For 304 foils, M_d is appropriately 55 °C [27]. Therefore, the tensile tests were also performed at an elevated temperature of 85 °C. Since the phase transformation takes place at RT rather than 85 °C for the tested foils, the effect of martensitic transformation was thus investigated by comparing the two scenarios. Also, to track the transformation kinetics from austenite to martensite during the micro-scaled deformation, the interrupted tensile tests at RT were conducted to different engineering strain levels including 0%, 10%, 20%, 30%, and fracture.

2.3. Measurement of martensite content

To evaluate the microstructure evolution of SUS304 foils at various strains, a reliable X-ray diffraction (XRD) method based on the integrated intensities of $(111)_\gamma$, $(200)_\gamma$, $(220)_\gamma$, $(311)_\gamma$, $(110)_{\alpha'}$, $(200)_{\alpha'}$, $(211)_{\alpha'}$, and $(220)_{\alpha'}$ diffraction peaks was adopted in the uniform deformation region [28]. The subscripts γ and α' represent diffraction peaks of austenite and martensite constituents, respectively. The intensity of the diffraction peak was evaluated by Rigaku D/max 2500PC XRD with CuK_α radiation. The XRD patterns were captured by the step-scanning from 35° to 100° as 2θ with an increment of 0.05°. Afterward, a quantitative estimation of martensite volume fraction was computed according to the fact that the entire integrated intensity of all diffraction peaks for an individual constituent in the aggregation is proportional to the volume fraction of the phase [29].

2.4. Numerical simulation

To validate the developed multiscale constitutive model and reveal the work-hardening mechanism, the finite element simulation based on the representative volume element (RVE)

was performed on the platform of ABAQUS. The microstructure morphology from the electron backscatter diffraction (EBSD) map of the 120 μm thick foil with the grain size of 60.3 μm was extracted by the Rhino software, and then the RVE model was established and imported in the ABAQUS software, as shown in Fig. 2 (a). The microstructure contains the hard martensite constituent, which is embedded within the soft austenite matrix. The mechanical behaviors of austenite and martensite were obtained by the multiscale constitutive model. The size of the RVE model was 50 × 50 μm, which initially contained 8.9% martensite islands randomly distributed in the 91.1% austenite matrix. Before fracture, the martensite content gradually increased to 28.3% due to the SIMT. In this model, the constraint equations were applied to the nodes on the right and bottom sides, and the symmetrical conditions were adopted on the left and upper sides to have equal displacements. The nodes at the bottom edge had the same displacement in the *y*-direction while they can freely move along the *x*-direction, and the nodes on the right side had the same displacement in the *x*-direction (parallel to the tensile direction). Four-node quadrilateral elements were chosen for the plane stress analysis of two-dimensional RVE. During the tensile deformation, the volume fraction of strain-induced martensite continuously increased with plastic strain, whereas the austenite matrix, in turn, decreased, as shown in Fig. 2 (b). In the finite element model, the continuous change of martensite volume fraction with plastic strain was realized by the USDFLD subroutine, which can redefine the user-defined field variables at the integration points. Different values of field variables were set to austenite and martensite. When the equivalent plastic strain value of integration points reached the set value, the material properties in the integration points were adjusted from austenite to martensite due to the change of the field variable.

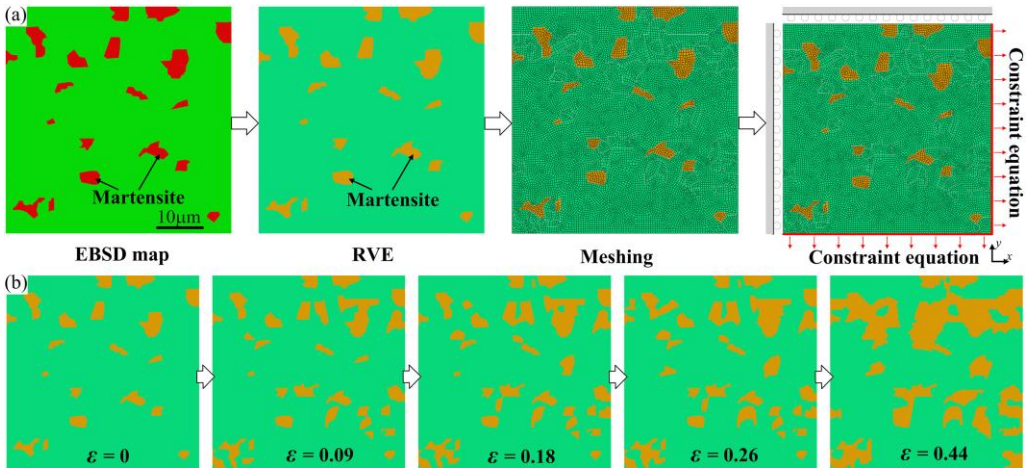

Fig. 2. Two-dimensional RVE model of the real microstructure: (a) finite element modeling

process and (b) strain-induced martensitic transformation in the finite element model.

3. Results and discussion

3.1. Size effect on strain-induced martensitic transformation

To explore both the geometric and grain size effects on SIMT, the XRD patterns were measured at diverse strain levels. Fig. 3 shows the XRD patterns of the foils annealed at 1000 ℃ as an example. It is found that the intensity of $(111)_{\gamma}$ diffraction peak gradually decreases and the intensity of $(110)_{\alpha'}$ diffraction peak gradually raises with the increase of strain level. This phenomenon mirrors that the SIMT occurs during plastic deformation. In addition, the diffraction peaks of martensite at 0% strain indicate that a small amount of martensite has already been generated during the furnace cooling, which is termed as annealing-induced martensitic transformation [30]. The appearance of annealing-induced martensite has been proved to be related to the sensitization phenomenon during annealing [31, 32], which leads to the precipitation or segregation of solute atoms and in turn increases the martensite start temperature M_s in local regions. The content of annealing-induced martensite was calculated using the XRD patterns. As presented in Fig. 4, the content of annealing-induced martensite increases with increasing grain size and decreasing foil thickness, which may be related to the influence of the size effect on sensitization.

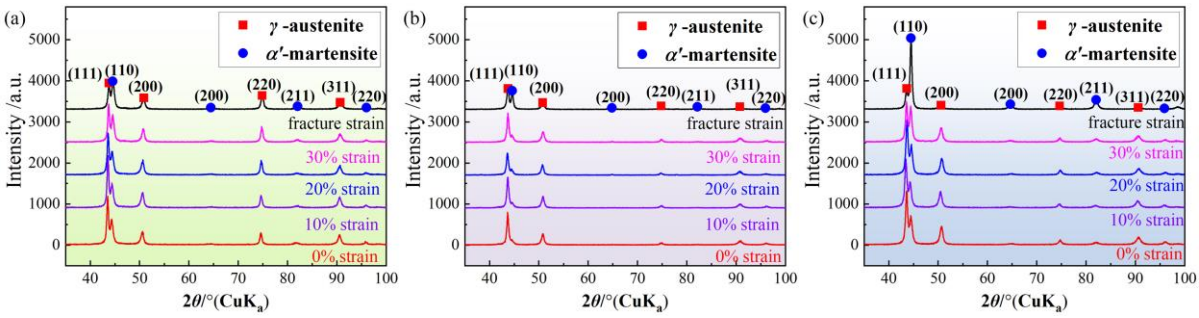

Fig. 3. XRD patterns of the deformed specimens annealed at 1000 ℃: (a) t = 50 μm, d = 21.3 μm, (b) t = 120 μm, d = 28.7 μm and (c) t = 200 μm, d = 29.5 μm.

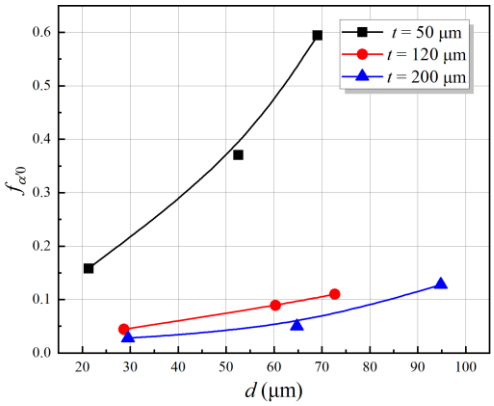

Fig. 4. Volume fraction of annealing-induced martensite $f_{\alpha'0}$ in diverse foils.

The volume fraction of strain-induced martensite was calculated by excluding the content of annealing-induced martensite, as given in Fig. 5. For a given foil thickness, the increase of grain size stimulates the generation of strain-induced martensite. In addition, the influence of foil thickness on SIMT was studied by comparing the content of deformation-induced martensite in 304 foils with identical grain size and different thicknesses. Since the 50 μm thick foils have more annealing-induced martensite, many martensitic embryos have formed before plastic deformation, which shortens the martensite nucleation process and further advances the martensite growth process. To avoid the effect of annealing-induced martensite on SIMT, the analysis of the effect of foil thickness on SIMT did not cover the 50 μm thick foils. Two sets of specimens with similar initial martensite content and grain size were selected to explore the geometric size effect on SIMT, as presented in Fig. 5 (d). It is found that the increase in foil thickness promotes the transformation from austenite to martensite, and the fine grain tends to weaken the effect of foil thickness on SIMT. Comparing the contents of strain-induced martensite in the 1400 μm thick sheet with a grain size of 48 μm [33] and the 120 μm thick foil with the grain size of 60.3 μm, the acceleration of SIMT with the increase of specimen thickness is also confirmed, as shown in Fig. 5 (b). Therefore, the increase of grain size and foil thickness can promote the SIMT of metastable metal foils during RT uniaxial tension.

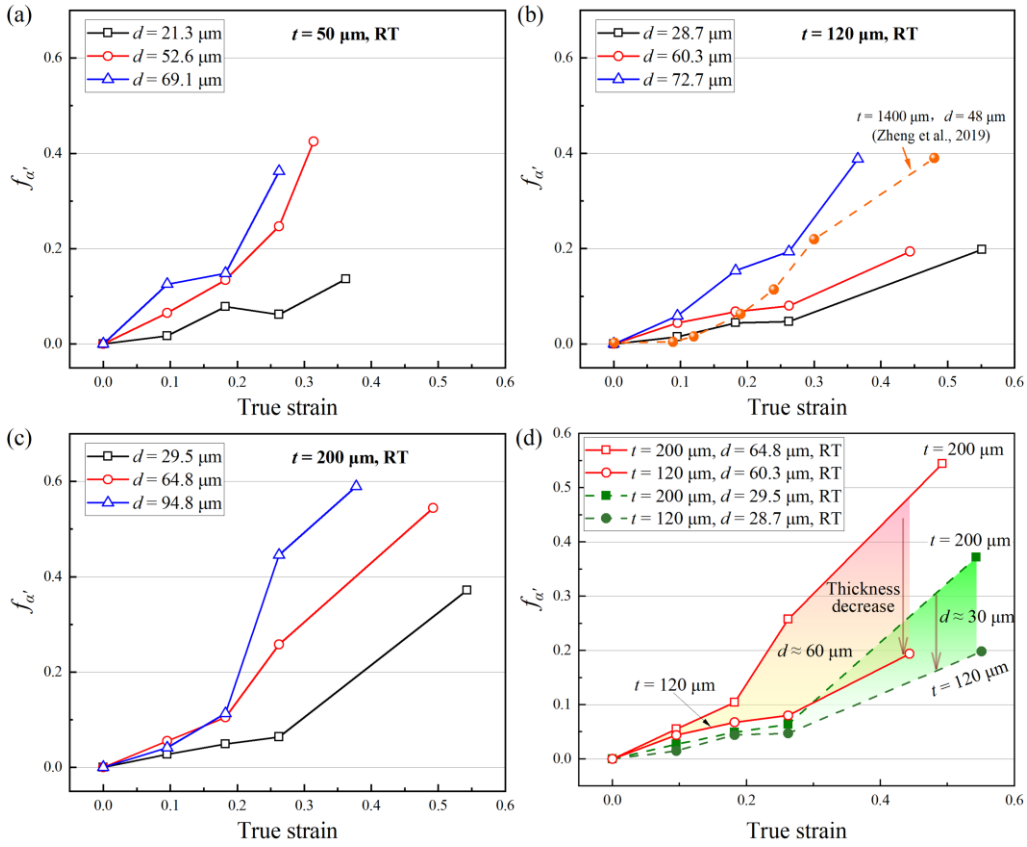

Fig. 5. Volume fraction of strain-induced martensite $f_{\alpha'}$ in metal foils: (a) t = 50 μm, (b) t = 120 μm, (c) t = 200 μm and (d) comparison between different thicknesses specimens with similar initial martensite content and grain size.

Fig. 6 depicts the impact mechanism of specimen thickness and grain size on SIMT. The atoms on the grain boundary are restricted by the neighboring atoms and hard to participate in the coordinated atom movement for martensitic transformation. Therefore, the grain refinement can strengthen the austenite matrix and hinder the shear transformation, thus delaying the trigger of SIMT [34]. In addition, the intersections of micro shear bands are acted as the dominant nucleation sites of martensitic embryos, where the micro shear bands include the bundles of stacking faults and deformation twins [35]. The micro shear bands near the grain boundary tend to migrate to the boundary and disappear, which results in the decrease of nucleation sites for the SIMT. Therefore, the SIMT is impeded by fine grains since the generation of nucleation sites is limited by grain boundaries. When the plastic strain reaches about 20%, the morphology of the formed martensite changes to a blocky irregular one due to the coalescence of martensitic embryos. Grain boundaries hinder the further growth of the blocky irregular martensite. It is concluded that grain boundaries enhance the stabilization of austenite, decrease the nucleation sites of martensite, and hinder the growth of

martensite, thereby inhibiting the SIMT. When the foil thickness decreases, the potential nucleation sites for the SIMT thereupon decrease due to the reduced fraction of grain interior. The SIMT is thus suppressed by the reduction in foil thickness. Therefore, the SIMT is dominated by the proportion of grain boundaries.

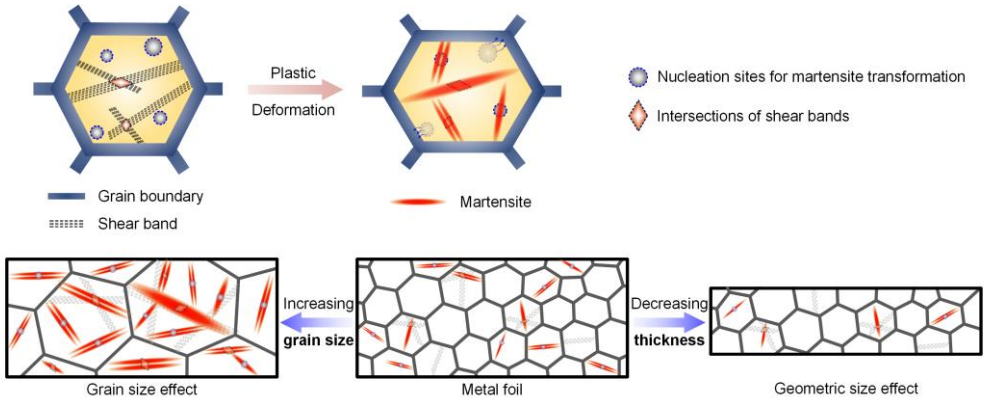

Fig. 6. Schematic diagram of the mechanism of size effect on strain-induced martensitic transformation.

3.2. Coupled influence of size effect and SIMT on deformation behavior

Fig. 5 showed that the increase of grain size and foil thickness can promote the SIMT of 304 foils during RT uniaxial tension. To reveal the coupled influence of size effect and size-dependent SIMT on deformation behavior, the true stress-strain responses of the foils deformed at RT and 85 °C are compared, as presented in Fig. 7. It is found the flow behavior of metastable foils presents two different patterns. Throughout the 85 °C deformation process, the specimens show an obvious size effect, i.e., the flow stress decreases with the decrease of thickness and increase of grain size. However, the stress of the specimens deformed at RT follows the typical size effect at the beginning and then exhibits noticeably increasing tendency due to the SIMT, especially when the strain exceeds 0.2. The increase of flow stress at RT is intensified with the growth of grain size and foil thickness since the SIMT is affected by both geometric and grain size effects. Moreover, the abnormal increase of flow stress of coarse-grained specimens tends to appear earlier than that of fine-grained specimens, and the subsequent flow stress is mainly controlled by the SIMT. The elongation of the foils decreases with the increase of grain size and the decrease of foil thickness regardless of the deformation temperature. This phenomenon mirrors that the elongation of metastable metal foils is still dominated by the size effect [36, 37] rather than the SIMT.

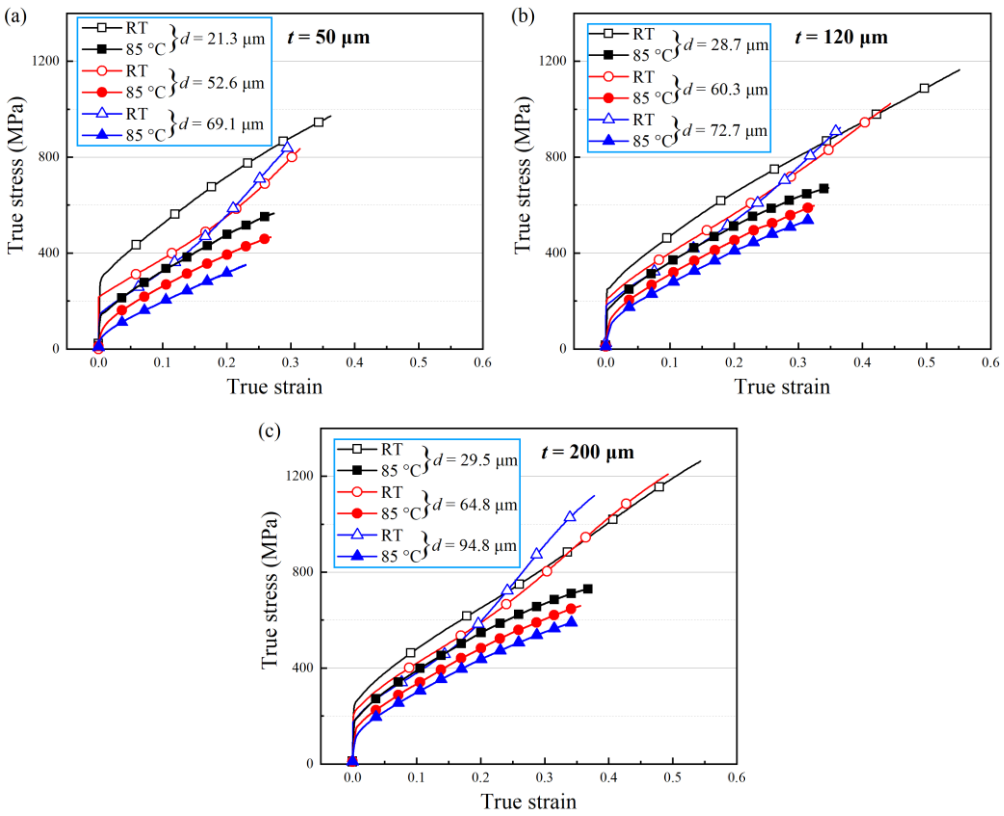

Fig. 7. True stress-strain responses of foils with various thicknesses at RT and 85 °C: (a) t = 50 μm, (b) t = 120 μm and (c) t = 200 μm.

The typical Hall–Petch equation [38] was adopted to describe the relation of the initial yield strength σ_y and the initial austenitic grain size d:

$$\sigma_y = \sigma_0 + k_{hp} d^{-1/2} \quad (1)$$

where σ_0 and k_{hp} are material constants. Fig. 8 depicts the Hall–Petch relation for the foils deformed at RT and 85 °C. The initial yield strength of the foils deformed at RT and 85 °C increases as the initial austenitic grain size decreases. This phenomenon reflects that metastable foils with the initial annealing-induced martensite also follow the Hall–Petch relation. The macro plastic deformation of 304 foils is attributed to the onset of plastic deformation of austenite, while the martensite phase is still in the elastic stage due to the higher yield strength [39]. Therefore, the austenite phase dominates the initial yield strength of 304 foils. As the advancement of macroscopic strain, the SIMT initiates, and the martensite starts plastic deformation under the drive of applied external stress and internal stress [39], thereby improving the strength of metastable foils. Therefore, the flow behavior of metastable foils is affected by the interplay of size effect and SIMT.

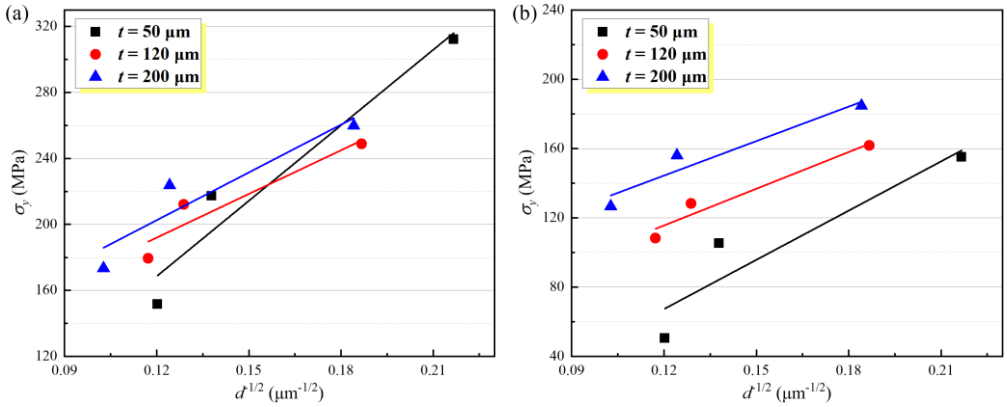

Fig. 8. Hall–Petch relation for metastable foils deformed at: (a) RT and (b) 85 °C.

To further describe the morphological transformation of the flow behavior of 304 foils under the interaction of size effect and SIMT, the corresponding work-hardening rates were computed and depicted in Fig. 9. The 200 μm thick foils present a work-hardening abnormality at RT similar to the previous work [40], which can be characterized as three stages. In stage I, the hardening rate drops sharply due to the initiation of dislocation glide. With the occurrence of SIMT, the work-hardening behavior is transferred from stage I to II. The work-hardening rate in stage II increases rapidly due to the dominant hardening effect of martensitic transformation. When the martensite volume fraction is close to saturation, the martensitic transformation rate drops rapidly, causing a fast decline of the work-hardening rate. The work-hardening behavior is transferred from stage II to III. The work-hardening behaviors of the 50 and 120 μm thick specimens are similar to that of the 200 μm thick specimens. Due to the restricted SIMT for the 50 and 120 μm thick specimens with fine grains, the weakening role of dislocation annihilation surpasses the combined hardening effect of SIMT and dislocation accumulation, resulting in a decrease of work-hardening rate in stage II and the absence of stage III.

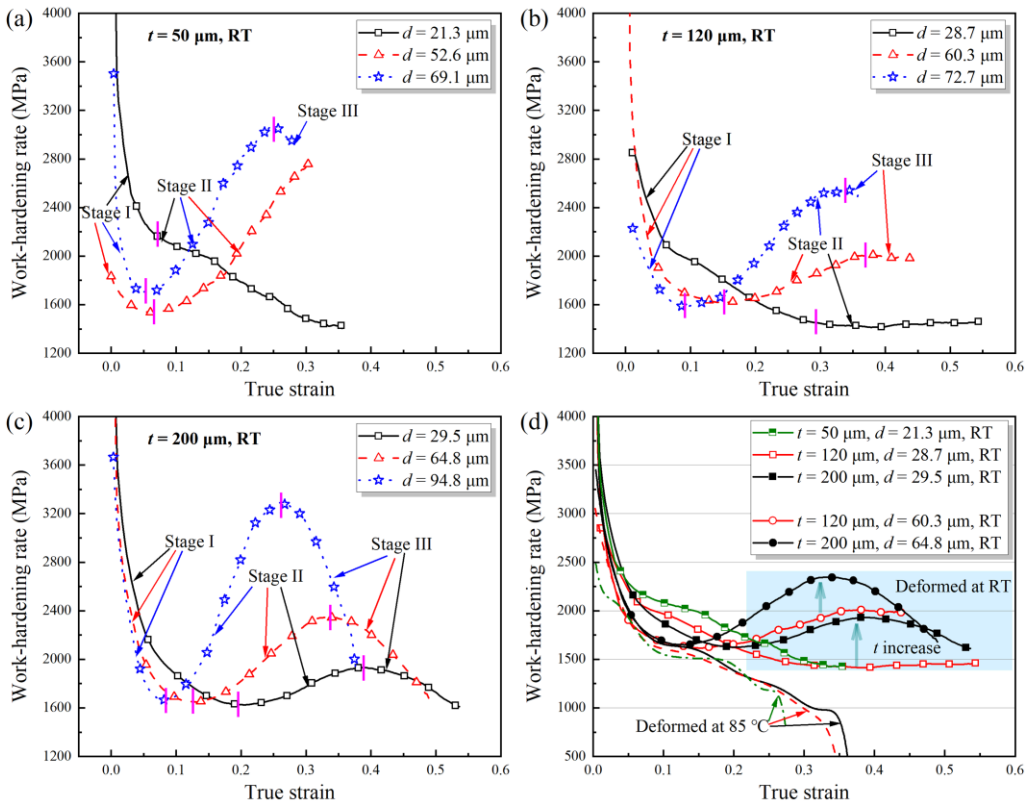

Fig. 9. Work-hardening behavior of 304 foils under diverse conditions: (a) t = 50 μm, (b) t = 120 μm, (c) t = 200 μm and (d) comparison between different thicknesses specimens with similar grain size.

The stain range of three stages and the magnitude of the increase in work-hardening rate are closely related to foil thickness and grain size. There is a clear trend that the strain range of stage I is shrunken with increasing grain size, i.e., the work-hardening behavior of coarse-grained foils during the deformation process is transferred from stage I to II earlier. The trend is caused by the fact that the increase of grain size accelerates the onset of SIMT. In addition, the work-hardening rate in stage II increases more rapidly with increasing grain size for a certain thickness and reaches a peak value prematurely. The early saturation of martensite in coarse-grained specimens leads to the shrinkage of stage II. The result confirms that the martensitic transformation rate is promoted by increasing grain size, in turn, resulting in an earlier onset and end of stage II and a faster increase in the work-hardening rate in stage II. Since the increase of geometric size can promote SIMT, the effect of foil thickness on the working-hardening rate is similar to the effect of grain size. As shown in Fig. 9 (d), the increase of foil thickness facilitates the work-hardening rate and advances the onset and end of stage II. The contribution of SIMT is gradually strengthened with the increase of foil thickness, resulting in the transformation of strain-hardening mode in stage II from decline

for the 50 μm thick foil to nearly constant for the 120 μm thick foil, and then to rise for the 200 μm thick foil. Comparing the hardening behavior of metal foils deformed at RT, the work-hardening at 85 ℃, which is only affected by the size effect, exhibits typical patterns due to the absence of SIMT.

4. Modeling and verification

4.1. Multiscale constitutive model considering size effect and SIMT

4.1.1. Martensitic transformation kinetic model

The martensite constituent in the metal foils consists of two types of martensite, viz., annealing-induced and strain-induced martensite, which can be formulated as:

$$f_M = f_{\alpha'0} + f_{\alpha'} \tag{2}$$

where f_M, $f_{\alpha'0}$, and $f_{\alpha'}$ are the volume fractions of the total, annealing-induced, and strain-induced martensite, respectively.

Some martensitic transformation kinetic models have been derived to reflect the volume fraction of strain-induced martensite $f_{\alpha'}$ in metastable ASSs, including the Olson and Cohen model [35], Gompertz model [41], and Logistic model [42]. Compared with the first two models, the Logistic model considers both the saturation of deformation-induced martensite and the physical process of SIMT, which is expressed as [42]:

$$f_{\alpha'} = \frac{f_s}{1+\exp\left(-\beta\left(\varepsilon-\varepsilon_m\right)\right)} \tag{3}$$

where f_s is the saturation volume fraction of martensite, β characterizes the martensitic transformation rate, ε is the true plastic strain, and ε_m is the strain value corresponding to 50% of the saturated level of martensite. The work-hardening rate drops rapidly in the later period of plastic deformation, implying that the rate of SIMT decreases and the content of deformation-induced martensite gradually saturates. Therefore, the value of f_s was replaced by the content of martensite after the fracture in the fitting process.

4.1.2. Constitutive models of austenite and martensite

Since the SIMT in the plastic deformation of SUS304 foils occurs at room temperature, the microstructure does not undergo dynamic recrystallization, and the grain number thus does not change during tension. The austenitic grain size gradually decreases with the decrease of the austenitic volume. Assuming that the austenitic grain has a spherical shape [24], the austenitic volume in the initial state and deformation process can be expressed as:

$$f_{\gamma 0} = \frac{\pi}{6} d^3 \times N \tag{4}$$

$$f_\gamma(\varepsilon) = \frac{\pi}{6} d_\gamma^3(\varepsilon) \times N \tag{5}$$

In Eq. (4), $f_{\gamma 0}$, d, and N denote the initial austenitic volume fraction, grain size, and grain number, respectively. In Eq. (5), $f_\gamma(\varepsilon)$ and $d_\gamma(\varepsilon)$ represent the instantaneous austenitic volume and grain size during plastic deformation, respectively. The instantaneous austenitic grain size can then be designated as:

$$d_\gamma(\varepsilon) = d \times \left(\frac{f_\gamma(\varepsilon)}{f_{\gamma 0}} \right)^{1/3} \tag{6}$$

where $f_{\gamma 0}$ and $f_\gamma(\varepsilon)$ can be calculated based on the content of martensite.

The plastic flow behavior of the austenitic phase in the metal foils can be characterized using Kocks–Mecking formalism, which can be used to describe the size effect on the mechanical deformation of metals and is written as follows [43]:

$$\sigma_\gamma = \sigma_{0\gamma} + \alpha M G_\gamma b_\gamma \sqrt{\rho} \tag{7}$$

$$\frac{d\rho}{M d\varepsilon_\gamma} = \frac{1}{b_\gamma d_\gamma(\varepsilon)} + \frac{k}{b_\gamma} \sqrt{\rho} - f\rho \tag{8}$$

where σ_γ and ε_γ are the true stress and plastic strain of austenite, respectively, $\sigma_{0\gamma}$ represents the lattice friction stress and the solid solution strengthening, α is a material parameter representing dislocation interactions, M is the Taylor factor, G_γ is the shear modulus for face-centered cubic, b_γ is the Burgers vector for face-centered cubic, and ρ is the forest dislocation density.

Eq. (8) reflects the variation of dislocation density with the true plastic strain of austenite. The first term on the right represents the contribution of grain boundaries to the geometrically necessary dislocations. The second term denotes the athermal storage of dislocation. The third one is the dislocation annihilation caused by dynamic recovery. k and f reflect the dislocation storage and annihilation rates, respectively.

The flow stress dependence of grain size has been well expressed by the Hall–Petch relation [38] in the following:

$$\sigma_\gamma = \sigma_{0\gamma} + k_{hp} d^{-1/2} \tag{9}$$

Comparing Eqs. (7) and (9), the initial dislocation density ρ_0 can be designated as a function of grain size d as below [44]:

$$\rho_0 = k_d d^{-1} \tag{10}$$

The combination of Eqs. (7), (8), and (10) is adopted to represent the constitutive behavior of austenite. The material parameters including k, f, and k_d needed to be fitted, and $\sigma_{0\gamma}$ in Eq. (7) can be theoretically estimated from an empirical equation [45]:

$$\sigma_{0_\gamma}\left(\mathrm{MPa}\right) = 68 + 354wt.\%\mathrm{C} + 20wt.\%\mathrm{Si} + 3.7wt.\%\mathrm{Cr} \tag{11}$$

Since $\sigma_{0\gamma}$ represents the initial stress associated with the presence of lattice friction and the solid solution strengthening, it was assumed that its value is not affected by the surface effect. In other words, the magnitude of $\sigma_{0\gamma}$ in the interior is the same as that at the surface layer.

On the other hand, the constitutive model established by Rodriguez et al. [46] was used to simulate the mechanical behavior of martensite in metal foils:

$$\sigma_{\alpha'} = \sigma_{0\alpha'} + \alpha M G_{\alpha'} \sqrt{b_{\alpha'}} \sqrt{\frac{1-\exp\left(-Mf\varepsilon_{\alpha'}\right)}{fL}} \tag{12}$$

where $\sigma_{\alpha'}$ and $\varepsilon_{\alpha'}$ are the true stress and plastic strain of martensite, $\sigma_{0\alpha'}$ represents the yield strength of the martensite phase, $G_{\alpha'}$ is the shear modulus for body-centered cubic, $b_{\alpha'}$ is the Burgers vector for body-centered cubic, and L is considered as the martensitic lath width. The yield strength of martensite in the interior, $\sigma_{0\alpha'i}$, is not influenced by the surface effect, which can be computed by the carbon content of the material by Eq. (14) [47]:

$$\sigma_{0\alpha'i}\left(MPa\right) = 461 + 1310\left(wt.\%\mathrm{C}\right)^{1/2} \tag{13}$$

In Eq. (12), L can be calculated by assuming that the austenite and martensite constituents have the same grain number [24]. Nevertheless, the increase of lath number rather than lath size of martensite in austenitic grains dominates the increase in martensite constituent. Therefore, L is considered as the dislocation mean free path in the martensite phase in this research. In the constitutive model of the martensite phase, the yield strength $\sigma_{0\alpha's}$ at the surface layer, L, and f are the fitted parameters to accurately determine the stress-strain behavior of martensite.

4.1.3. Modeling coupled mixture law with surface layer model

The stress-strain mixture law has been widely used to describe the macroscopic deformation behavior of dual-phase steels and even multiphase steels because of its simplicity and applicability. A stress mixture law was proposed by Gladman et al. [48] using a power-law volume fraction function designated as:

$$\sigma\left(\varepsilon\right) = \left(1 - f_2^{\,n}\right)\sigma_1\left(\varepsilon\right) + f_2^{\,n}\sigma_2\left(\varepsilon\right) \tag{14}$$

where $\sigma(\varepsilon)$, $\sigma_1(\varepsilon)$, and $\sigma_2(\varepsilon)$ are the stresses of the overall, soft phase, hard phase, respectively. The parameter f_2 denotes the volume fraction of the hard phase. The difference in strain between different phases is included in the value of n, which is usually set to be 1 or 2. However, the parameter n is related to the strength ratio of austenite to martensite and the martensitic transformation rate during the plastic deformation of metastable ASS, which makes the value of n relevant to plastic strain [25]. An intermediate mixture law [49] is more appropriate for describing the mechanical behavior of metastable ASSs than the Gladman-type mixture law, which is expressed as follows:

$$\begin{aligned} \sigma(\varepsilon) &= \left(1-f_M(\varepsilon)\right)\sigma_\gamma\left(\varepsilon_\gamma\right) + f_M(\varepsilon)\sigma_{\alpha'}\left(\varepsilon_{\alpha'}\right) \\ \varepsilon &= \left(1-f_M(\varepsilon)\right)\varepsilon_\gamma + f_M(\varepsilon)\varepsilon_{\alpha'} \end{aligned} \tag{15}$$

where $\sigma_\gamma(\varepsilon_\gamma)$ and $\sigma_{\alpha'}(\varepsilon_{\alpha'})$ are the stresses of austenite and martensite, respectively, ε_γ and $\varepsilon_{\alpha'}$ are the strains of austenite and martensite when the overall strain is ε, respectively. An iso-work hypothesis [50], i.e., the mechanical work increment is taken equally in each constituent regardless of the material state, is utilized to avoid the arbitrary stress-strain distribution between two phases, which is expressed as follows:

$$\sigma_\gamma\left(\varepsilon_\gamma\right)d\varepsilon_\gamma = \sigma_{\alpha'}\left(\varepsilon_{\alpha'}\right)d\varepsilon_{\alpha'} \tag{16}$$

The combination of Eqs. (15) and (16) is used to represent the allocation of strain and stress in austenite and martensite at a certain macro strain.

Considering that the surface and interior grains have different mechanical properties, the kinetic model of SIMT and the constitutive models of austenite and martensite were substituted into the intermediate mixture law with the iso-work hypothesis to fit the overall stress-strain curves of metastable ASSs almost completely composed of the surface or interior layers. The constitutive parameters of austenite and martensite at the surface or interior layers were thus determined. However, most metal foils are composed of the surface and interior grains, whose flow stress is denoted as [51]:

$$\sigma(\varepsilon) = \eta\sigma_s(\varepsilon) + (1-\eta)\sigma_i(\varepsilon) \tag{17}$$

where $\sigma_s(\varepsilon)$ and $\sigma_i(\varepsilon)$ are the flow stresses of the surface and interior layers, respectively. η represents the proportion of the surface layer, which can be denoted as:

$$\eta = \frac{N_s}{N} = \frac{d}{t}\cdot\frac{2\left(w+t-2d\right)}{w} \tag{18}$$

where N is the total number of grains, N_s is the surface grain number, and w is the foil width.

The volume fraction and constitutive model of austenite and martensite are expressed in

vector forms:

$$\mathbf{f}=\begin{pmatrix}1-f_M(\varepsilon)\\ f_M(\varepsilon)\end{pmatrix}$$

$$\boldsymbol{\sigma}=\begin{pmatrix}\sigma_\gamma(\varepsilon_\gamma)\\ \sigma_{\alpha'}(\varepsilon_{\alpha'})\end{pmatrix}=\begin{pmatrix}\sigma_{0\gamma}+\alpha MG_\gamma b_\gamma\sqrt{\rho(\varepsilon_\gamma)}\\ \sigma_{0\alpha'}+\alpha MG_{\alpha'}\sqrt{b_{\alpha'}}\sqrt{\dfrac{1-\exp(-Mf\,\varepsilon_{\alpha'})}{fL}}\end{pmatrix} \tag{19}$$

Assuming that martensite is evenly distributed in the material, the martensite volume fraction of the surface and interior layers is the same. According to the intermediate mixture law, the flow stress of the surface layer is obtained:

$$\sigma_s(\varepsilon)=\mathbf{f}^T\boldsymbol{\sigma}_s \tag{20}$$

Similarly, the flow stress of the interior layer is calculated as follows:

$$\sigma_i(\varepsilon)=\mathbf{f}^T\boldsymbol{\sigma}_i \tag{21}$$

By substituting Eqs. (20) and (21) into Eq. (17), the multiscale model is constructed as below:

$$\sigma(\varepsilon)=\eta\mathbf{f}^T\boldsymbol{\sigma}_s+(1-\eta)\mathbf{f}^T\boldsymbol{\sigma}_i \tag{22}$$

The constructing process for the multiscale constitutive model is also described in Appendix A in the form of a flowchart.

4.2. Mechanical behaviors of austenite and martensite

To verify the validity of the multiscale model, the mechanical responses of austenite and martensite at the surface and interior layers need to be determined first. The flow stresses of austenite and martensite at the surface layer can be derived from the experimental data of the 120 μm thick foil with the grain size of 60.3 μm and the 200 μm thick foil with the grain size of 94.8 μm, which are entirely composed of the surface layer ($t/d \approx 2$). The stress-strain curves and the martensite volume fractions obtained by the Logistic model of these two sets of foil were substituted into the intermediate mixture law with the iso-work hypothesis to fit the constitutive parameters (Eqs. (7), (8), (10), and (12)) of the surface austenite and martensite. On the other hand, the experimental data of the 1400 μm thick foil with the grain size of 48 μm [33], which is almost entirely composed of the interior layer ($t/d \approx 29$), was chosen to achieve the constitutive parameters of the interior austenite and martensite. Since the martensite constituent is still in the stage of elastic deformation when austenite begins to yield, the elastic stage of martensite was thus added in the fitting process. The elastic modulus of martensite was assumed to be consistent with that of austenite, which was set as

199 GPa. Table 3 lists the input parameters for the calibration.

Table 3 Input parameters for the constitutive models of austenite and martensite.

Parameters	Value	Source
$\sigma_{0\gamma}$ (MPa)	163	Eq. (11)
$\sigma_{0\alpha' i}$ (MPa)	750	Eq. (13)
α	0.4	
M	3	
G_{γ} (MPa)	72000	Ref. [24]
$G_{\alpha'}$ (MPa)	78500	
b_{γ} (mm)	2.58×10^{-7}	
$b_{\alpha'}$ (mm)	2.48×10^{-7}	

Table 4 summarizes the fitted constitutive parameters via the global optimization algorithm, and the identified mechanical behaviors of austenite and martensite at the surface and interior layers are presented in Fig. 10. The flow stress of the individual phase demonstrates that the martensite has a high yield strength than the austenite matrix, which causes a significant increase in flow stress with plastic strain. Compared with the interior austenite, the surface austenite has a higher dislocation annihilation rate since the dislocations are easy to slip out of the free surface. A more obvious difference is that the surface austenite has less initial dislocation density, which can be attributed to the fact that the mechanical properties of surface grains are rather similar to a single crystal and the grain boundary strengthening is negligible [51]. This quasi-single crystalline status leads to a lower deformation resistance of the surface austenite. On the other hand, the yield strength of the martensite constituent significantly decreases at the surface layer, and the surface martensite has a larger dislocation mean free path than the interior one. The less dislocation density at the surface layer may bring about a reduction in the dislocation density in the transformed martensite at the surface, resulting in lower yield strength and a larger dislocation mean free path. According to the proposed multiscale constitutive model, the given macro stress-strain point (ε, σ) corresponds to two micro stress-strain points, i.e., the point (ε_{γ}, σ_{γ}) for austenite and the point ($\varepsilon_{\alpha'}$, $\sigma_{\alpha'}$) for martensite, as shown in Fig. 10. The difference of stress-strain responses in austenite and martensite constituents implies a must for partitioning the stress-strain data between different constituents.

Table 4 Fitted parameters in the multiscale model considering size effect and SIMT.

Phase	Parameters	Value (Surface)	Value (Interior)
Austenite	k	0.009	0.009
	f	0.055	0.043
	k_d ($\times 10^6$ mm^{-1})	0.2	2.582
Martensite	σ_0 (MPa)	327	–
	f	0.002	0.0017
	L (mm)	0.003	0.0025

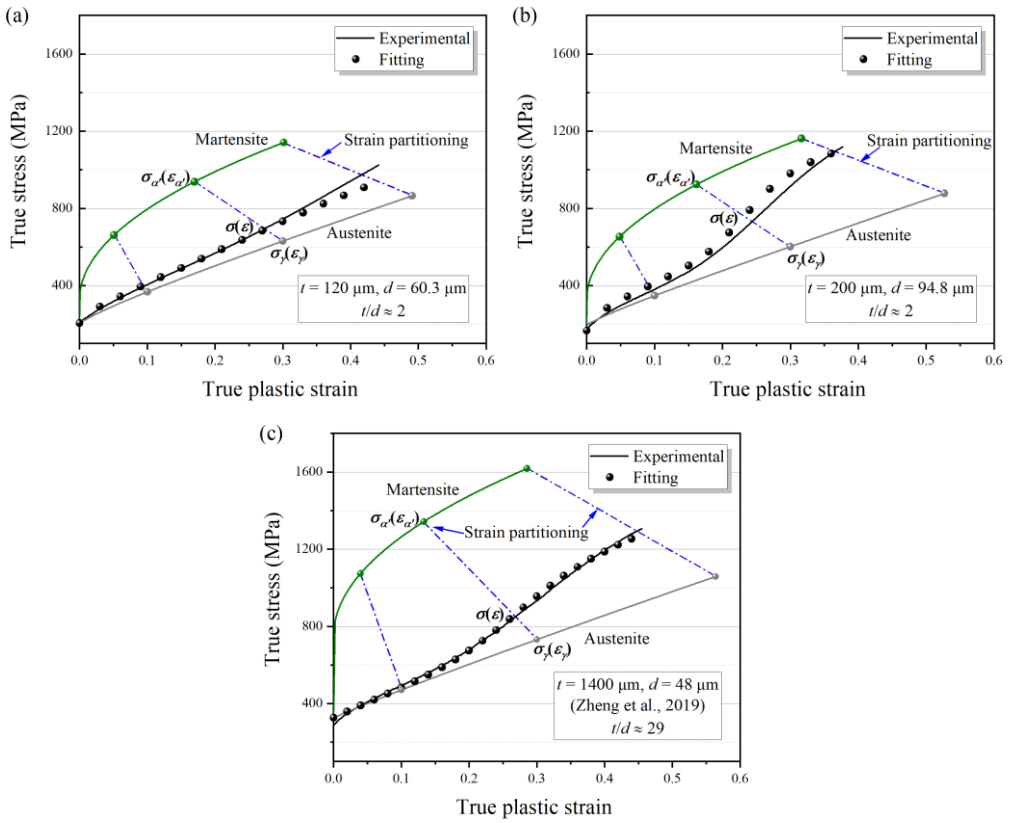

Fig. 10. Stress-strain responses and strain partitioning for austenite and martensite at different material conditions: (a) t = 120 μm, d = 60.3 μm, (b) t = 200 μm, d = 94.8 μm and (c) t = 1400 μm, d = 48 μm [33].

4.3. Verification of multiscale constitutive model

Due to the coupled impact of the size effect and the SIMT, the instability of 304 foil is significantly aggravated. The experimental data under all material conditions were used to confirm the validity of the established multiscale model. The comparison between the experimental flow stress curves and the ones predicted by the multiscale constitutive model is presented in Fig. 11. The results demonstrated that the multiscale constitutive model

considering martensitic transformation and size effect is valid for characterizing the deformation behavior of metastable metal foils with micron-sized grains at $t/d \geq 2$. It is also found that the flow stress of quasi-single crystalline state ($t/d \leq 1$) is overestimated by the multiscale model, as shown in Fig. 11 (b~c). The multiscale model is proposed based on the surface layer model, and the surface layer model does not consider the scenario of $t/d < 2$. Furthermore, the solid solution strengthening is restricted due to the severe sensitization in the annealing process for the 50 μm thick foils with the grain sizes of 52.6 and 69.1 μm, resulting in an obvious decrease in flow stress. In addition, the deformation behavior of the quasi-single crystalline is strongly dependent on the individual grain size, shape, and orientation, which is not considered in the multiscale constitutive model.

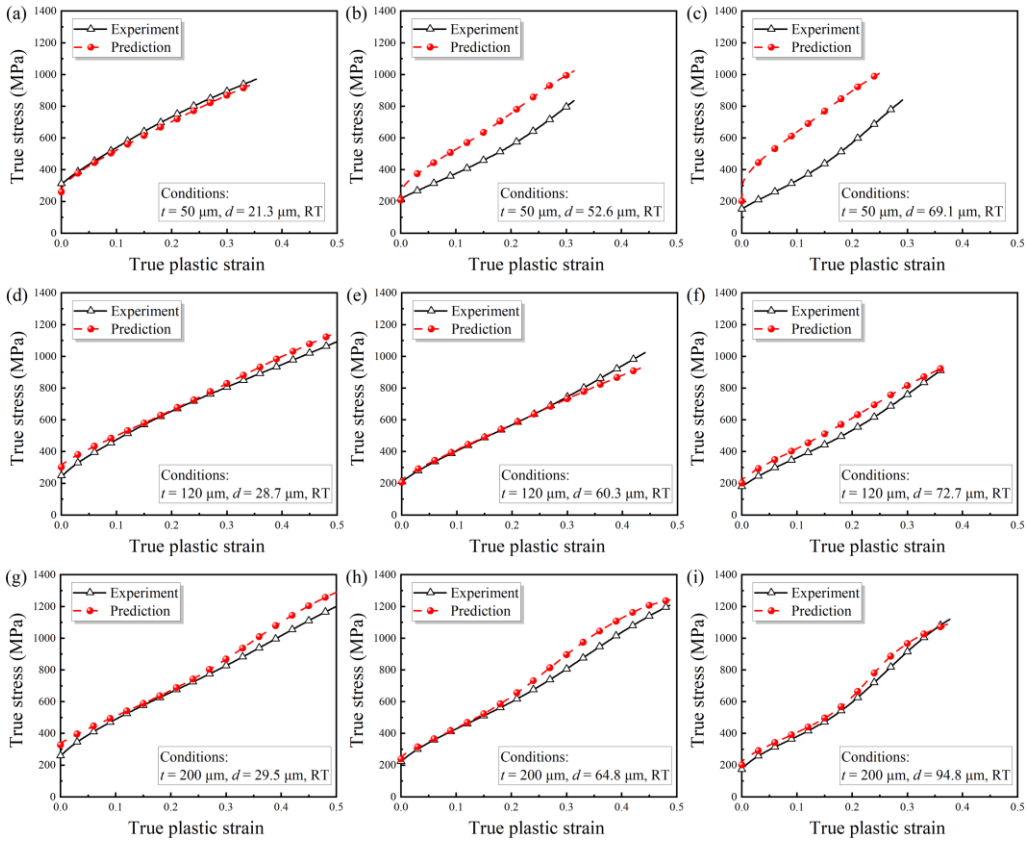

Fig. 11. Model validation by comparing the experimental results and the predicted ones for metal foils with different states: (a~c) t = 50 μm, (d~f) t = 120 μm and (g~i) t = 200 μm.

Meanwhile, the root mean square deviations (RMSD) between the experimental data and the predictive results in terms of stress level and work-hardening rate were used to evaluate the applicability of the developed multiscale constitutive model:

$$\mathrm{RMSD}=\sqrt{\frac{\sum_{i=1}^{n}\left(\hat{x}_i - x_i\right)^2}{n}} \tag{23}$$

where $\hat{x}_i$ and x_i are the predicted and experimental results, respectively. The values of RMSD under different material conditions are shown in Fig. 12. It is observed that the disparity between the experimental curves and predictive ones is aggravated with reducing specimen thickness and rising grain size. In addition, the prediction deviation reaches the maximum value at $t/d \leq 1$, which remains to be further studied.

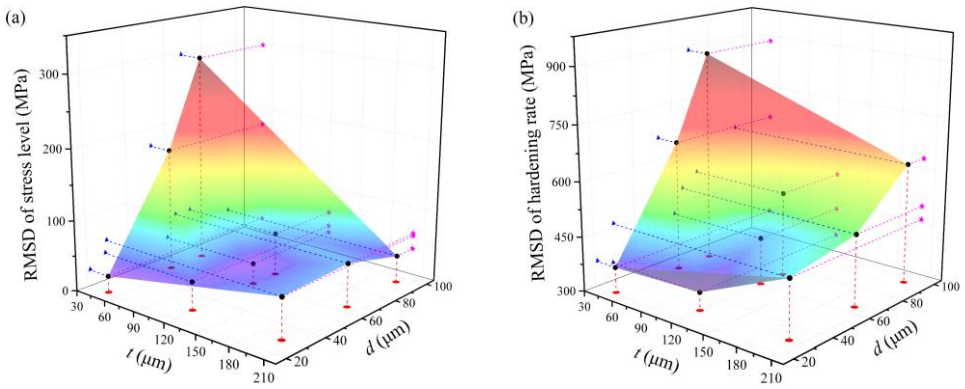

Fig. 12. Root mean square deviations (RMSD) analysis of the experiment results and the predictive ones for (a) flow stress and (b) work-hardening rate.

In addition, the mechanical behaviors of austenite and martensite were used to numerically simulate the uniaxial tension process to verify the validation of the model and further reveal the hardening mechanism during the deformation. Fig. 13 depicts the simulation results of metal foil with the thickness of 120 μm and the grain size of 60.3 μm. It is seen from Fig. 13 (a) that the work-hardening is intensified by the continuous increase of martensite content with plastic strain. The overall stress-strain curve obtained by simulation coincides well with the experimental one, which verifies the validation of the multiscale constitutive model.

Fig. 13 (b~d) present the microscopic strain distribution of austenite and martensite mixture at the macroscopic equivalent plastic strains of 0.1, 0.2, and 0.3, respectively. It is found that the specimen is deformed heterogeneously and the deformation is concentrated in the austenite matrix. Whereas, the martensite islands (blue area) are considered as hard nondeformable dispersions embedded within the soft austenite matrix. The heterogeneous plastic deformation at the interface between austenite and martensite is formed to maintain the compatibility between austenite and martensite, as shown with red regions in Fig. 13 (b~d). The geometrically necessary dislocations are generated at the austenite and martensite interface to accommodate the heterogeneous plastic deformation, which strengthens the kinetic constraints to the matrix and leads to a dispersion hardening effect [52]. As the deformation advances, the martensite volume fraction increases and the martensite phase

starts to plastically deform to accommodate the shape change, which further enhances the dispersion hardening effect and in turn increases the work-hardening rate.

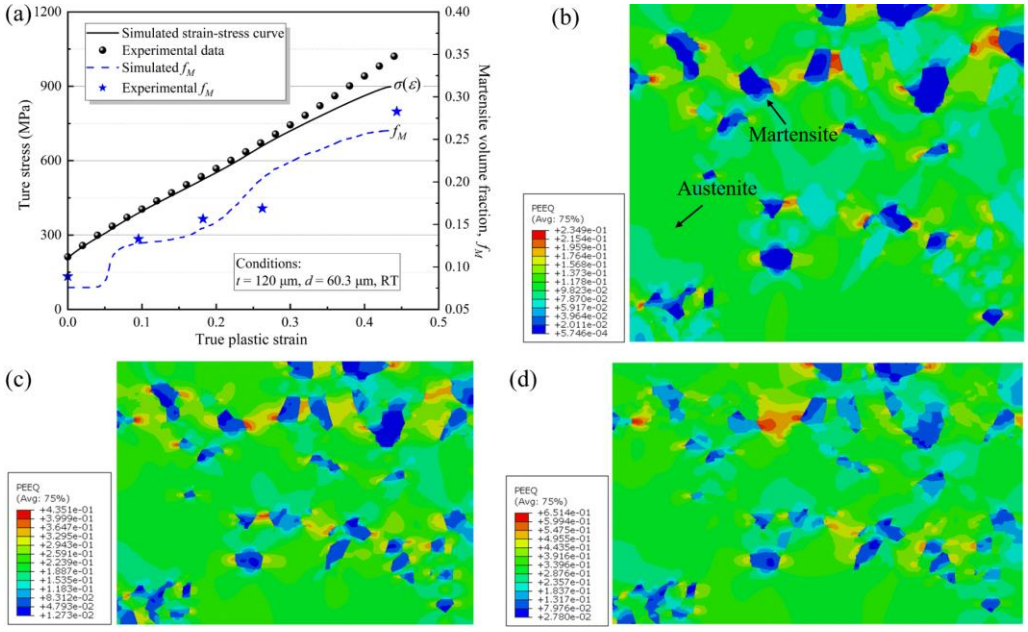

Fig. 13. Simulation for verifying the multiscale constitutive model and revealing the hardening mechanism: (a) comparison between simulation and experiment and (b~d) microscopic strain distributions at different macroscopic levels: (b) ε = 0.1, (c) ε = 0.2 and (d) ε = 0.3.

5. Conclusions

In this research, the size-dependence strain-induced martensitic transformation (SIMT) and unique hardening behavior in micro-scaled deformation of metastable austenitic foils were explored. To further understand the unique deformation behavior, a multiscale constitutive model considering the coupled influence of size effect and SIMT was developed. The work-hardening mechanism of austenite and martensite aggregation was thus revealed through finite element simulation and physical examination. The main conclusions are summarized in the following:

(1) A small amount of martensite is produced during the annealing, which is attributed to the sensitization phenomenon that increases the martensite start temperature M_S in local regions. The SIMT is impeded by the decrease of grain size and foil thickness because the nucleation and growth of martensite are restricted by the increase of grain boundary.

(2) The flow behavior of metastable foils at room temperature is affected by the interplay of size effect and SIMT. The martensitic transformation rate is promoted by increasing grain size and foil thickness, in turn, resulting in an earlier onset and end of stage

II and a faster increase in the work-hardening rate in stage II.

(3) The austenite and martensite phases at the interior layer have greater deformation assistance and work-hardening rate than those at the surface layer due to the surface effect. The established multiscale constitutive model considering the coupled influence of martensitic transformation and size effect is validated to be able to characterize and predict the plastic deformation behavior of metal foils with micron-sized grains at $t/d \geq 2$.

(4) The dispersion hardening effect of metastable foils is caused by the heterogeneous plastic deformation of austenite and martensite aggregation. With the increase of plastic strain, the martensite volume fraction increases and the martensite phase starts to plastically deform to accommodate the shape change, which further enhances the dispersion hardening effect and in turn increases the work-hardening rate.

(5) The validity of the developed multiscale constitutive model is verified by physical experiment and finite element simulation. The model represents the correlation among martensitic transformation kinetics, size effect, and dislocation density-based constitutive description of each phase, and can be used for controlling and tailoring of microstructure in micro-scaled deformation of metastable foils.

Acknowledgments

The authors deeply acknowledge the support from the National Natural Science Foundation of China (Grant Nos.: 51975031, 51635005, 51835011, and 51575465) and Defense Industrial Technology Development Program (No.: JCKY2018601C207).

Appendix A. Constructing process for the multiscale constitutive model

Fig. A1 gives a detailed constructing process for the multiscale constitutive model coupling the strain-induced martensitic transformation with the size effect. First, the suitable kinetic model of strain-induced martensitic transformation, the constitutive models of austenite and martensite, and the intermediate mixture law were evaluated and selected. Subsequently, the phase transformation kinetic model and the constitutive models of austenite and martensite were imported into the intermediate mixture law to fit the overall stress-strain curves of metastable austenite stainless steels almost completely composed of the surface or interior layer grains. The constitutive parameters of austenite and martensite at the surface and interior layers were thus determined. Finally, the multiscale constitutive model was constructed by coupling the surface layer model, the intermediate mixture law, the phase transformation kinetic model, and the constitutive models of individual phases at the surface and interior layers.

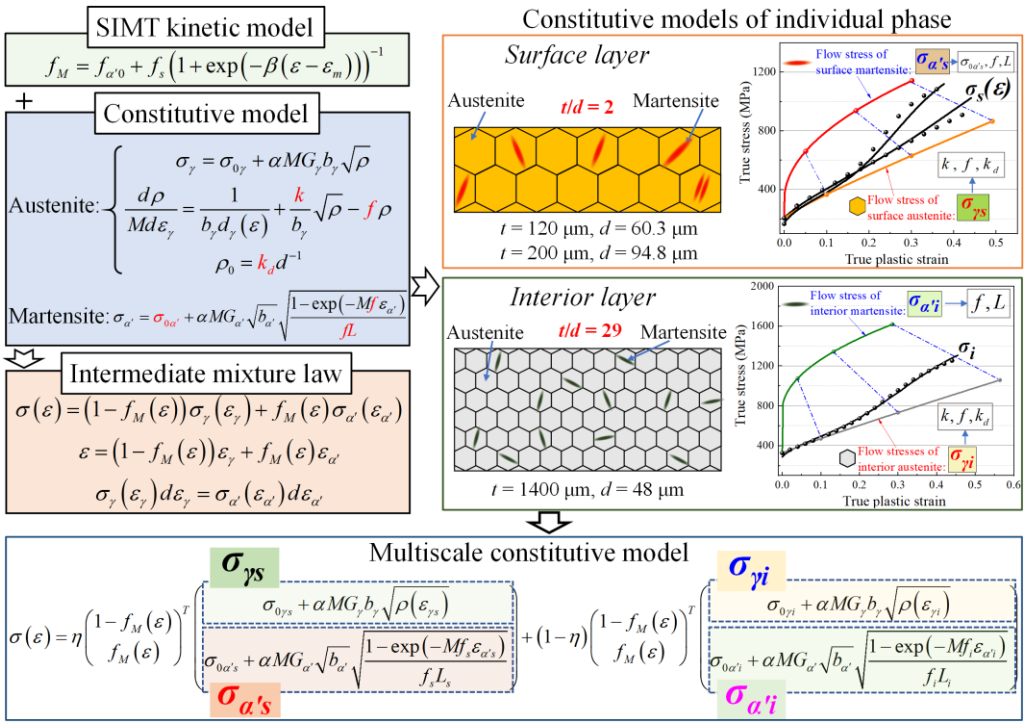

Fig. A1 Development framework of the multiscale constitutive model.

References

[1] M.W. Fu, J.L. Wang, A.M. Korsunsky, A review of geometrical and microstructural size effects in micro-scale deformation processing of metallic alloy components, International Journal of Machine Tools and Manufacture, 109 (2016) 94-125.
[2] X.F. Tang, S.Q. Shi, M.W. Fu, Interactive effect of grain size and crystal structure on deformation behavior in progressive micro-scaled deformation of metallic materials, International Journal of Machine Tools and Manufacture, 148 (2020) 103473.
[3] Q. Zheng, T. Shimizu, M. Yang, Grain size effect on mechanical behavior of thin pure titanium foils at elevated temperatures, International Journal of Mechanical Sciences, 133 (2017) 416-425.
[4] B. Meng, M.W. Fu, Size effect on deformation behavior and ductile fracture in microforming of pure copper sheets considering free surface roughening, Materials & Design, 83 (2015) 400-412.
[5] B. Meng, W.H. Wang, Y.Y. Zhang, M. Wan, Size effect on plastic anisotropy in microscale deformation of metal foil, Journal of Materials Processing Technology, 271 (2019) 46-61.
[6] J. Shi, B. Meng, C. Cheng, M. Wan, Size effect on the subsequent yield and hardening behavior of metal foil, International Journal of Mechanical Sciences, 180 (2020) 105686.
[7] B. Meng, M. Wan, R. Zhao, Z. Zou, H. Liu, Micromanufacturing technologies of compact heat exchangers for hypersonic precooled airbreathing propulsion: A review, Chinese Journal of Aeronautics, (2020).
[8] B. Jia, A. Rusinek, R. Pesci, S. Bahi, R. Bernier, Thermo-viscoplastic behavior of 304 austenitic stainless steel at various strain rates and temperatures: Testing, modeling and validation, International Journal of Mechanical Sciences, 170 (2020) 105356.
[9] S.K. Varma, J. Kalyanam, L.E. Murk, V. Srinivas, Effect of grain size on deformation-induced martensite formation in 304 and 316 stainless steels during room temperature tensile testing, Journal of Materials Science Letters, 13 (1994) 107-111.
[10] V. Shrinivas, S.K. Varma, L.E. Murr, Deformation-induced martensitic characteristics in 304 and 316 stainless steels during room-temperature rolling, Metallurgical and Materials Transactions A, 26 (1995) 661-671.
[11] J. Gu, L. Zhang, S. Ni, M. Song, Effects of grain size on the microstructures and mechanical properties of 304 austenitic steel processed by torsional deformation, Micron, 105 (2018) 93-97.
[12] Y. Matsuoka, T. Iwasaki, N. Nakada, T. Tsuchiyama, S. Takaki, Effect of grain size on thermal and mechanical stability of austenite in metastable austenitic stainless steel, ISIJ international, 53 (2013) 1224-1230.
[13] A. Kisko, R.D.K. Misra, J. Talonen, L.P. Karjalainen, The influence of grain size on the strain-induced martensite formation in tensile straining of an austenitic 15Cr–9Mn–Ni–Cu stainless steel, Materials Science and Engineering: A, 578 (2013) 408-416.
[14] R.D.K. Misra, P.K.C. Venkatsurya, M.C. Somani, L.P. Karjalainen, Nanoscale Deformation Behavior of Phase-Reversion Induced Austenitic Stainless Steels: The Interplay Between Grain Size from Nano-Grain Regime to Coarse-Grain Regime, Metallurgical and

Materials Transactions A, 43 (2012) 5286-5297.
[15] V.S.A. Challa, X.L. Wan, M.C. Somani, L.P. Karjalainen, R.D.K. Misra, Strain hardening behavior of phase reversion-induced nanograined/ultrafine-grained (NG/UFG) austenitic stainless steel and relationship with grain size and deformation mechanism, Materials Science and Engineering: A, 613 (2014) 60-70.
[16] J.-T. Gau, P.-H. Chen, H. Gu, R.-S. Lee, The coupling influence of size effects and strain rates on the formability of austenitic stainless steel 304 foil, Journal of Materials Processing Technology, 213 (2013) 376-382.
[17] D.M. Xu, X.L. Wan, J.X. Yu, G. Xu, G.Q. Li, Effect of grain refinement on strain hardening and fracture in austenitic stainless steel, Materials Science and Technology, 34 (2018) 1344-1352.
[18] W.Q. Mao, S. Gao, W. Gong, M.H. Park, Y. Bai, A. Shibata, N. Tsuji, Influence of Grain Size on Work-Hardening Behavior of Fe-24Ni-0.3C Metastable Austenitic Steel, in, Springer International Publishing, Cham, 2018, pp. 95-98.
[19] M. Naghizadeh, H. Mirzadeh, Effects of Grain Size on Mechanical Properties and Work-Hardening Behavior of AISI 304 Austenitic Stainless Steel, Steel Research International, 90 (2019) 1900153.
[20] M.I. Latypov, S.R. Kalidindi, Data-driven reduced order models for effective yield strength and partitioning of strain in multiphase materials, Journal of Computational Physics, 346 (2017) 242-261.
[21] E.-Y. Kim, W. Woo, Y.-U. Heo, B. Seong, J. Choi, S.-H. Choi, Effect of kinematic stability of the austenite phase on phase transformation behavior and deformation heterogeneity in duplex stainless steel using the crystal plasticity finite element method, International Journal of Plasticity, 79 (2016) 48-67.
[22] M. Zhang, H. Chen, Y. Wang, S. Wang, R. Li, S. Li, Y.-D. Wang, Deformation-induced martensitic transformation kinetics and correlative micromechanical behavior of medium-Mn transformation-induced plasticity steel, Journal of Materials Science & Technology, 35 (2019) 1779-1786.
[23] A. Perlade, O. Bouaziz, Q. Furnémont, A physically based model for TRIP-aided carbon steels behaviour, Materials Science and Engineering: A, 356 (2003) 145-152.
[24] J. Bouquerel, K. Verbeken, B.C. De Cooman, Microstructure-based model for the static mechanical behaviour of multiphase steels, Acta Materialia, 54 (2006) 1443-1456.
[25] B. Fu, W.Y. Yang, Y.D. Wang, L.F. Li, Z.Q. Sun, Y. Ren, Micromechanical behavior of TRIP-assisted multiphase steels studied with in situ high-energy X-ray diffraction, Acta Materialia, 76 (2014) 342-354.
[26] W.J. Dan, Z.Q. Lin, S.H. Li, W.G. Zhang, Study on the mixture strain hardening of multi-phase steels, Materials Science and Engineering: A, 552 (2012) 1-8.
[27] H. Wang, Y. Jeong, B. Clausen, Y. Liu, R.J. McCabe, F. Barlat, C.N. Tomé, Effect of martensitic phase transformation on the behavior of 304 austenitic stainless steel under tension, Materials Science and Engineering: A, 649 (2016) 174-183.
[28] A.K. De, D.C. Murdock, M.C. Mataya, J.G. Speer, D.K. Matlock, Quantitative

measurement of deformation-induced martensite in 304 stainless steel by X-ray diffraction, Scripta Materialia, 50 (2004) 1445-1449.
[29] Y.F. Shen, X.X. Li, X. Sun, Y.D. Wang, L. Zuo, Twinning and martensite in a 304 austenitic stainless steel, Materials Science and Engineering: A, 552 (2012) 514-522.
[30] M.J. Sohrabi, M. Naghizadeh, H. Mirzadeh, Deformation-induced martensite in austenitic stainless steels: A review, Archives of Civil and Mechanical Engineering, 20 (2020) 124.
[31] J.K. Kim, Y.H. Kim, B.H. Lee, K.Y. Kim, New findings on intergranular corrosion mechanism of stabilized stainless steels, Electrochimica Acta, 56 (2011) 1701-1710.
[32] S. Takaya, T. Suzuki, Y. Matsumoto, K. Demachi, M. Uesaka, Estimation of stress corrosion cracking sensitivity of type 304 stainless steel by magnetic force microscope, Journal of Nuclear Materials, 327 (2004) 19-26.
[33] C. Zheng, H. Jiang, X. Hao, J. Ye, L. Li, D. Li, Tailoring mechanical behavior of a fine-grained metastable austenitic stainless steel by pre-straining, Materials Science and Engineering: A, 746 (2019) 332-340.
[34] J.-E. Jin, Y.-S. Jung, Y.-K. Lee, Effect of grain size on the uniform ductility of a bulk ultrafine-grained alloy, Materials Science and Engineering: A, 449 (2007) 786-789.
[35] G.B. Olson, M. Cohen, Kinetics of strain-induced martensitic nucleation, Metallurgical Transactions A, 6 (1975) 791.
[36] C. Cheng, M. Wan, B. Meng, M.W. Fu, Characterization of the microscale forming limit for metal foils considering free surface roughening and failure mechanism transformation, Journal of Materials Processing Technology, 272 (2019) 111-124.
[37] M.W. Fu, W.L. Chan, Micro-scaled products development via microforming, Springer, 2014.
[38] E. Hall, The deformation and ageing of mild steel: III discussion of results, Proceedings of the Physical Society. Section B, 64 (1951) 747.
[39] S. Zhang, P. Wang, D. Li, Y. Li, In situ investigation on the deformation-induced phase transformation of metastable austenite in Fe–13% Cr–4% Ni martensitic stainless steel, Materials Science and Engineering: A, 635 (2015) 129-132.
[40] A.K. De, J.G. Speer, D.K. Matlock, D.C. Murdock, M.C. Mataya, R.J. Comstock, Deformation-induced phase transformation and strain hardening in type 304 austenitic stainless steel, Metallurgical and Materials Transactions A, 37 (2006) 1875-1886.
[41] S.S.M. Tavares, J.M. Pardal, M.J.G. da Silva, H.F.G. Abreu, M.R. da Silva, Deformation induced martensitic transformation in a 201 modified austenitic stainless steel, Materials Characterization, 60 (2009) 907-911.
[42] P.M. Ahmedabadi, V. Kain, A. Agrawal, Modelling kinetics of strain-induced martensite transformation during plastic deformation of austenitic stainless steel, Materials & Design, 109 (2016) 466-475.
[43] C. Keller, E. Hug, Kocks-Mecking analysis of the size effects on the mechanical behavior of nickel polycrystals, International Journal of Plasticity, 98 (2017) 106-122.
[44] Y.Z. Liu, M. Wan, B. Meng, Multiscale modeling of coupling mechanisms in electrically

assisted deformation of ultrathin sheets: An example on a nickel-based superalloy, International Journal of Machine Tools and Manufacture, 162 (2021) 103689.
[45] F.B. Pickering, Physical metallurgy and the design of steels, Applied Science Publishers, 1978.
[46] R. Rodriguez, I. Gutierrez, Unified formulation to predict the tensile curves of steels with different microstructures, Materials Science Forum, 426-4 (2003) 4525-4530.
[47] M. Cohen, The Strengthening of steel, Trans. AIME, 224 (1962) 638-657.
[48] T. Gladman, I.D. Mclvor, F.B. Pickering, Some aspects of the structure-property relationships in high-carbon ferrite-pearlite steels, Journal of the Iron and Steel Institute, 210 (1972) 916-930.
[49] I. Tamura, Y. Tomota, H. Ozawa, Proc. 3rd Int. Conf. Strength of Metals and Alloys, Cambridge, 1 (1973) 611.
[50] O. Bouaziz, P. Buessler, Mechanical behaviour of multiphase materials : an intermediate mixture law without fitting parameter, Revue de Métallurgie, 99 (2002) 71-77.
[51] X. Lai, L. Peng, P. Hu, S. Lan, J. Ni, Material behavior modelling in micro/meso-scale forming process with considering size/scale effects, Computational materials science, 43 (2008) 1003-1009.
[52] Z.Y. Cai, B. Meng, M. Wan, X.D. Wu, M.W. Fu, A modified yield function for modeling of the evolving yielding behavior and micro-mechanism in biaxial deformation of sheet metals, International Journal of Plasticity, 129 (2020) 102707.